Technology in Cancer Research & Treatment
ISSN 1533-0346
Volume 2, Number 6, December (2003)

Instrumentation for Multi-modal Spectroscopic Diagnosis of Epithelial Dysplasia

www.tcrt.org

James W. Tunnell, Ph.D.[1]
Adrien E. Desjardins, B.S.[1]
Luis Galindo, B.S.[1]
Irene Georgakoudi, Ph.D.[2]
Sasha A. McGee, B.S.[1]
Jelena Mirkovic, B.S.[1]
Markus G. Mueller, Ph.D.[1]
Jon Nazemi, M.S.[1]
Freddy T. Nguyen, B.S.[1]
Adam Wax, Ph.D.[3]
Qingguo Zhang, Ph.D.[1]
Ramachandra R. Dasari, Ph.D.[1]
Michael S. Feld, Ph.D.[1,*]

[1]G.R. Harrison Spectroscopy Laboratory
Massachusetts Institute of Technology
77 Massachusetts Ave., Bldg 6-014
Cambridge, MA 02139
[2]Wellman Laboratories of Photomedicine
Department of Dermatology
Massachusetts General Hospital
40 Blossom Street, WEL 224
Boston, MA 02114
[3]Department of Biomedical Engineering
Duke University
Box 90281
Durham, NC 27708-0281

* Corresponding Author:
Michael S. Feld, Ph.D.
Email: msfeld@mit.edu

Reflectance and fluorescence spectroscopies have shown great promise for early detection of epithelial dysplasia. We have developed a clinical reflectance spectrofluorimeter for multimodal spectroscopic diagnosis of epithelial dysplasia. This clinical instrument, the FastEEM, collects white light reflectance and fluorescence excitation-emission matrices (EEM's) within a fraction of a second. In this paper we describe the FastEEM instrumentation, designed for collection of multi-modal spectroscopic data. We illustrate its performance using tissue phantoms with well defined optical properties and biochemicals of known fluorescence properties. In addition, we discuss our plans to develop a system that combines a multi-spectral imaging device for wide area surveillance with this contact probe device.

Introduction

Over 85% of all cancers originate in the epithelium, a layer of highly cellular tissue covering the inner and outer surfaces of the body. Cancers of epithelial origin are generally preceded by a precursor lesion known as dysplasia. Pathological characteristics of epithelial dysplasia include nuclear atypia, cellular proliferation and alterations in architecture. Pathological examination of biopsy specimens of dysplastic tissue shows characteristic morphologic changes in cell nuclei, which are hallmarks of dysplasia. The nuclei become enlarged, crowded, and hyperchromatic (abnormally darkly stained). Although the gross and microscopic appearance of dysplasia in different organs and different types of epithelium can vary significantly, these morphological features are common to all types of dysplasia. Identification of dysplasia is particularly important because most such lesions are readily treatable if diagnosed at an early, noninvasive stage. However, many forms of dysplasia are difficult to detect and diagnose using current methods.

Current screening methods usually involve visual inspection of suspicious tissue sites. Subsequent invasive biopsy may then be required. Biopsy specimens are analyzed histopatholigically for markers of dysplasia and malignancy, which include metabolic activity, epithelial thickness, stromal architecture (depth and density), and nuclear morphology (size, density, and shape). This detection method is problematic for two reasons: i) dysplasia is not always detectable by visual inspection, so numerous unnecessary tissue biopsies are taken and ii) dysplasia can be difficult to diagnose, as evidenced by low inter-observer agreement (1-4).

Therefore, there is a need for minimally-invasive techniques to determine the disease state of tissue. Optical techniques offer a method to gain morphological and biochemical information. Light delivery and collection are performed minimally-invasively via optical fibers, which can be brought into contact with the tissue surface either externally or via an endoscopic channel. In addition, opti-

cal radiation is non-ionizing. Optical instrumentation is generally inexpensive, portable and compact, making it adaptable to the clinical setting.

Numerous optical techniques have been explored for obtaining structural and functional information from tissues. Steady-state diffuse reflectance (5-8) and frequency domain photon migration (9) suggest that optical scattering and absorption change with the progression of disease. Endogenous fluorescence spectroscopy has been shown to provide information about the biochemical composition of tissue (10) and has been used to detect dysplasia in the uterine cervix (11, 12), adenomatous colon polyps (5, 13), the esophagus (6,14) and the oral cavity (15, 16). Laser scanning confocal microscopy (LSCM) can be used to create both reflected light and fluorescence 3D high resolution video rate images within tissue (17). Two-photon microscopy (TPM) can image fluorophores deep within a tissue sample (18). Optical coherence tomography (OCT) has had great success in obtaining cross-sectional images of human tissues *in vivo* (19). Each of these techniques provides a unique tissue parameter (biochemical, structural, or morphological) that can be used to characterize tissue and aid the pathologist in diagnosing disease.

It stands to reason that a combination of such techniques can provide complimentary diagnostic information about the tissue. Indeed, a new technique, tri-modal spectroscopy (TMS) (6, 7, 16), combines three spectroscopic modalities to provide biochemical, structural, and morphological information simultaneously. Diffuse reflectance spectroscopy (DRS) provides information about the morphology and biochemistry of the stromal tissue determining values of the absorption and reduced scattering coefficients, $\mu_a(\lambda)$ and $\mu_s'(\lambda)$, respectively (5). Light scattering spectroscopy (LSS) determines epithelial nuclear size distribution and density. Intrinsic fluorescence spectroscopy (IFS) yields the relative contributions of endogenous tissue fluorophores (e.g., NADH and collagen).

Diffuse reflectance spectroscopy uses a mathematical model based on the diffusion approximation of light propagation in tissue (5). The model provides the wavelength dependent scattering parameter, $\mu_s'(\lambda)$, as well as the hemoglobin concentration and oxygen saturation. Because this technique analyzes diffusely reflected light, it generally measures properties of the bulk tissue (i.e., the thick stromal layer).

Light scattering spectroscopy uses the reflectance spectra to assess the morphology of the epithelium (20). The spectral component of the singly backscattered light contains information on nuclear size distribution and density within the epithelium; however, singly backscattered light makes up only a small fraction (2-5%) of the reflectance spectrum. The collected reflectance spectrum contains both diffuse reflectance (multiply scattered) and singly backscattered light. Extraction of the singly backscattered spectrum can be achieved by subtracting the diffuse reflectance component (20) from the total collected reflectance spectrum. The resulting singly backscattered spectrum exhibits an oscillatory behavior in wavelength space, the frequency of which can be used to extract the size distributions of the epithelial cell nuclei. This technique has been used clinically to provide the percentage of enlarged nuclei, the number density of nuclei, and the standard deviation in the nuclear size in several organs (esophagus, colon, uterine cervix, oral cavity, and bladder) (7, 21). These studies have found that nuclear size and crowding increase with the progression of dysplasia, which agrees well with findings of pathology.

The collected fluorescence and reflectance spectra can be used to extract the intrinsic fluorescence spectra (i.e., the fluorescence unaffected by tissue absorption and scattering) (22-24). Fluorescence photons generated within the tissue are scattered and absorbed during their path to the tissue surface, where they are collected via the optical fiber probe. Therefore, the intensity and lineshape of the collected fluorescence spectra can be significantly distorted, making difficult the extraction of biochemical composition of the tissue from the measured signal. This is a particular problem in the presence of absorbers such as hemoglobin. Because the reflectance spectrum undergoes similar absorption and scattering events, information contained within the reflectance spectra can be used to extract the intrinsic fluorescence from the collected fluorescence spectra (5). IFS can then be used to obtain relative concentrations of fluorophores within mucosal tissues (12). Studies in the uterine cervix and oral cavity have shown that collagen fluorescence decreases from normal to dysplastic to cancerous tissue sites. These changes could be the result of differences in the levels of expression of enzymes such as matrix metalloproteinases (MMPs), a class of enzymes responsible for stromal matrix degradation. Differences in the levels and/or patterns of expression of MMP-2 and other proteases involved in carcinogenesis have been reported between normal squamous epithelium, squamous metaplasia and squamous intraepithelial lesions (SIL) (25). Additionally, an increase in the NADH fluorescence is noted for the cancerous/dysplastic oral tissue sites as compared to the normal sites and in the cervical SIL's compared to that of the squamous metaplasia sites. This increase could result from an increased number of epithelial cells and/or their metabolic activity. These types of biochemical changes may precede any morphological changes within the tissue, opening the possibility for very early detection of dysplasia.

Each of these spectroscopic techniques probes a different and complementary tissue parameter. While each technique alone can distinguish normal, dysplastic, and cancerous tissues with fairly high degree of sensitivity and specificity, the

combination of all three techniques in a tri-modal configuration results in a superior diagnosis. This has been demonstrated in a set of pilot studies in the esophagus (6), uterine cervix (7), and the oral cavity (16).

These pilot studies have provided a solid basis for multi-modal spectroscopic diagnosis of epithelial dysplasia. However, we note that in all three cases mentioned above, data analysis has been performed off-line, and has been time consuming. Indeed, one great advantage of such a spectral diagnosis is to provide a real-time diagnosis.

We have developed a clinical instrument that collects these three types of spectroscopic data and provides the means to implement a real-time diagnosis. This instrument is an improvement on the system described by Zangaro *et al*. (26) that was used in the TMS studies outlined above, and a further development of the instrument introduced by Muller *et al*. (27) This new instrument collects white light reflectance and fluorescence excitation-emission (EEM's) within a fraction of a second. In this system, we have devised a method to accurately collect the white light reflectance spectrum over a broad wavelength range (300-800 nm as opposed to the previous 350-700 nm). This increase in spectral range is important for the accurate acquisition of LSS signals. In addition, the new instrument extends the lower excitation wavelength down to 308 nm from 347 nm, making it possible to study new tissue fluorophores, such as tryptophan. This system is controlled by a compact, portable computer with a custom software interface that allows for easy implementation of data analysis routines, making it possible to implement real-time data analysis and diagnosis. In this paper, we describe this instrument, designed for collection of multi-modal spectroscopic data in general, and tri-modal spectroscopy (combination of DRS, LSS, and IFS) in particular. We illustrate its performance using tissue phantoms with well defined optical properties and biochemicals of known spectroscopic properties. In addition, we describe development of a system that combines a multi-spectral imaging device for wide-area surveillance with this contact probe device. The development of real-time analysis and diagnostic algorithms as well as clinical results will be discussed elsewhere.

System Description

The FastEEM (fast excitation-emission matrix) reflectance spectrofluorimeter is a clinical device that collects two types of tissue spectra: i) laser-induced fluorescence excitation-emission spectra and ii) white light reflectance spectra. This portable reflectance spectrofluorimeter (Figure 1) collects EEM's and reflectance spectra in a fraction of a second. Because the FastEEM system employs pulsed light sources and gated detection, motion artifacts and distorting effects of ambient light are eliminated. These features make it compatible for use in standard clinical procedures, where white light illumination is always present (e.g., in the case of endoscopy). Light collection and delivery are achieved via an optical fiber probe that is small enough to be introduced into the accessory channel of an endoscope. The following sections describe the opto-mechanical system, the probe design, and the software control of the system.

Opto-mechanical System

The FastEEM delivers a sequence of ten laser pulses (308-480 nm) and two white light pulses to the tissue via an optical fiber probe (see below for details of the probe design). The same probe collects the white light reflectance and fluorescence and delivers it to the entrance slit of the diffraction grating spectrometer (Spectra Pro 150, Acton Research, Acton, MA), where it is dispersed onto an intensified CCD detector (PIMAX, Roper Scientific, Princeton, NJ). The CCD is operated in a gated mode, where the intensifier is biased on for only the short period of time (~30 μs) immediately prior to and after each laser/white light pulse. The short duration of this gate ensures that the background from ambient light is negligible. All ten laser-induced emission spectra and the two white light reflectance spectra are collected in approximately 0.3 s. Several of these acquisitions can be averaged together to increase the signal-to-noise ratio (SNR). We have found that the acquisition of five measurements provides sufficient SNR in most tissues, making a typical acquisition time on the order of 1.5 s.

This short acquisition time is achieved using a set of rapidly rotating wheels (Figure 2) driven by an AC motor at just over 3 Hz (180 RPM). The laser lines between 342-480 nm are generated using a set of dye lasers, while the 308 nm laser line comes directly from a XeCl excimer laser (8 ns pulse FWHM, Optex XeCl, Lambda Physik, Ft. Lauderdale, FL). The two white light spectra are generated using a Xe flashlamp (L7684, 1J @ 2.9 μs pulse FWHM, Hammamatsu Corp., Bridgewater, NJ). The twelve separate positions on each wheel are illustrated in Figure 1(b). The "dye cell wheel" has nine dye cells with different dye solutions, one prism, and two open spaces. The dye cells are 2.8 ml spectrosil quartz cuvettes (Starna Cells, Atascadero, CA) with a 10 mm pathlength and transmission from 170-2700 nm. Dye solutions are a mixture of the dyes shown in Table I and a solvent (either p-dioxane or methanol). As each dye cell traverses the common optical resonant cavity (mirrors M1 and M2), it is pumped by the XeCl excimer laser. The output pulses are directed through a 10% reflective mirror (M1) and lens (L3) into the laser excitation fiber of the optical fiber probe. In addition, as the prism traverses the optical cavity, the XeCl excimer laser is triggered and the laser pulse is redirected into the laser excitation fiber. The two open spaces in the wheel are reserved for white light excitation. When these positions traverse the optical cavity, the excimer laser is not trig-

gered. Rather, the Xe flashlamp is triggered and focused (L4) into a white light excitation fiber. The white light and the laser excitation fibers are combined into one fiber and guided to the optical fiber probe. As the collected light returns through the collection fibers, it is focused onto the entrance slit of the spectrograph. The "filter wheel" spins in synchronization with the dye cell wheel. This filter wheel holds the long pass filters that remove the excitation line from the collected light.

The FastEEM collects two white light reflectance spectra to obtain an accurate reflectance spectrum over the broad wavelength range from 300-800 nm. The white light source has significant intensity from 270 nm to greater than 800 nm. The spectrograph operates in the first order of diffraction, so that the longest wavelength it can collect is twice the shortest wavelength, providing a range from 270-540 nm. In order to avoid light in the second order of diffraction above 540 nm, the FastEEM collects a second reflectance spectrum using a long pass filter (420 nm) to remove the short wavelengths. The amplitude of the filtered spectral response is adjusted in software to match that of the unfiltered response in the region between 460 and 530 nm, and these two white light spectra are merged (at 500 nm) to create one continuous spectrum from 300-800 nm.

The timing of the data collection is achieved through the use of a timer controller. This controller consists of a control logic circuit and a National Instruments timer/counter board (PCI-6602, National Instruments, Austin, TX). Optical interrupters (Omron Photomicrosensors EE-SX770, Schaumburg, IL) are used to generate trigger signals from pins mounted on the rotating wheel. The timer controller uses these trigger signals to determine when to pulse the laser or white light source and when to gate and read data from the detector.

Probe Design

The fiber optic probe resembles a flexible catheter with an overall length of over 3 m and a diameter of approximately 1.2 mm (Figure 3(a)). This small diameter enables it to be inserted in the accessory channel of a standard endoscope. The distal tip consists of seven 200 μm core multimode optical fibers (NA = 0.22) (in a six around one configuration, Figure 3(b)) which are fused together to form an optical shield approximately 1 mm long. The central fiber transmits the excitation light, while the six surrounding fibers collect light from the tissue and deliver it back to the entrance slit of the spectrograph. This arrangement of fibers and quartz shield provide a fixed geometry of overlapping excitation and collection cones, creating a sampling spot on the tissue surface with a diameter of approximately 800 μm. The quartz shield is beveled at 17° to reduce internal reflections from the probe-air interface. The proximal end of the catheter is terminated at seven SMA connectors, allowing for simple and quick changing of the optical fiber probes. One SMA connector leads to an optical fiber beam-splitter, where one fiber is split into two for each of the excitation sources. This greatly simplifies the alignment of the system in that the white light and the laser light can be aligned separately. The remaining six collection fibers lead from the SMA connector to the entrance slit of the spectrograph, where they are arranged linearly and parallel to the slit. The quartz shield in this probe design allows for the collection of tissue fluorescence and diffusely scattered light as well as light scattering in a small range of angles in the backward direction.

Table I
Technical specifications for the FastEEM laser dyes.

Laser Dye	Center wavelength [nm]	FWHM [nm]
p-Terphenyl (PTP)	342	9
PBD	360	8
Exalite 384	383	7
Exalite 398	400	7
LD 425	407	8
Stilbene 420	425	12
Coumarin 440	441	8
Coumarin 460	461	8
Coumarin 480	483	9

Software Control and Data Calibration

All systems of the FastEEM are controlled from a portable computer using custom software developed in the graphical programming environment LabView 7.0 (National Instruments, Austin, TX). Data acquisition can be initialized either by pressing a push-key within the program or by using a footswitch, providing control to the physician acquiring the data. In addition, the control software handles all data calibration, enabling on-line (i.e., real-time) data acquisition and calibration. This helps provide an immediate check as to the data quality. Background calibration is used to remove effects of CCD dark currents and stray light. The wavelength is calibrated by recording a spectrum from a mercury lamp. The intensity of each dye laser is inherently different from one another, and the individual dye laser intensities vary slightly from day to day due to optical alignment and dye degradation. We correct each EEM for excitation intensity by measurement of a standard rhodamine B dye mixture (5 g/L, ethylene-glycol). The known quantum yields of rhodamine B are then used to correct the intensity of each emission spectrum. White light reflectance is calculated by dividing the background corrected tissue spectrum by that of a reflectance standard (20% reflectance standard, Labsphere Inc., North Sutton, NH).

System Performance

Light Source Specifications

The light source output specifications of the FastEEM are listed in Table II. These specifications were measured at the

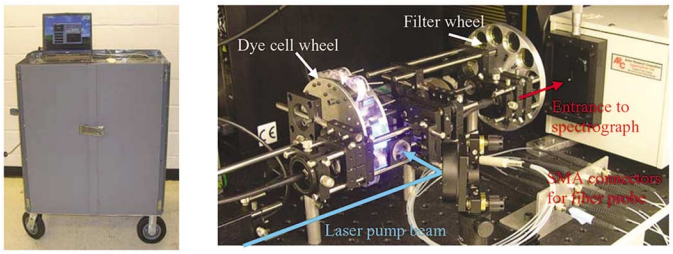

Figure 1: FastEEM reflectance spectrofluorimeter. (**a**) Full clinical instrument. (**b**) The dye cell and filter wheels that provide the laser sources for the laser induced fluorescence measurement.

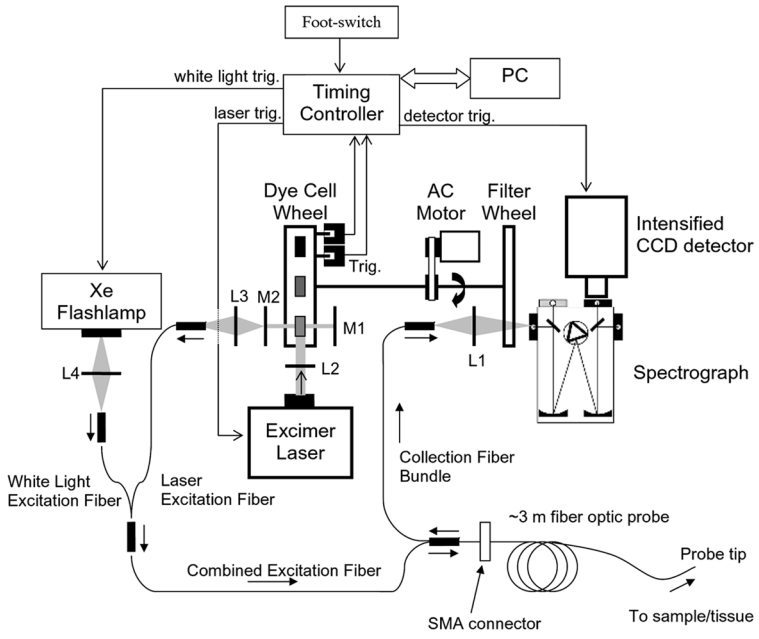

Figure 2: Schematic layout of the FastEEM clinical spectrophotometer. L1, L2, L3, L4 are lenses. M1 and M2 are mirrors.

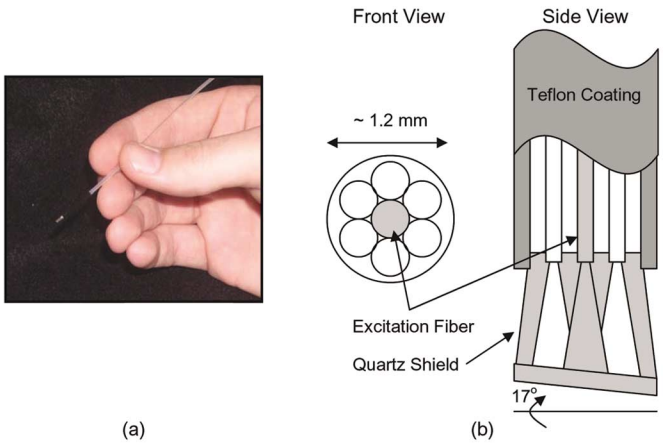

Figure 3: (**a**) Photograph and (**b**) schematic diagram of the distal tip of the optical fiber probe.

Table II
Light source characteristics of the FastEEM as measured at the output of the optical fiber probe.

	Lasers	White Light
Wavelength range	308 – 480 nm	240 – 2000
Pulse Energy (max.)	15 µJ	5 µJ
Pulse Width	8 ns	2.9 µs
Repititon Rate	30 Hz	6 Hz
Spot Size (dia.)	800 µm	800 µm
Fluence (0.5 mm dia. spot)	7.7 mJ/cm^2	2.5 mJ/cm^2
Average Power	230 mW/cm^2	15 mW/cm^2
Peak Power	960 kW/cm^2	860 W/cm^2

output of the optical fiber probe. The center wavelength and the full width at half maximum (FWHM) for each of the laser dyes are listed in Table I, and the lineshapes of each of the laser lines are shown in Figure 4.

The spectral response of the Xe flashlamp reflected from the 20% reflectance standard is shown in Figure 5. The bold line indicates the corrected lamp spectrum (i.e., the lamp spectrum free from distortions due to light diffracted in the second order). Also shown are the spectral response of the 420 nm long pass filtered Xe flashlamp and the spectral response of the unfiltered flashlamp. Note that the only difference between the spectral response of the corrected Xe flashlamp and the unfiltered flashlamp is the small region between 550-800 nm, where the unfiltered spectrum is slightly above the corrected spectrum. This increase in intensity in the unfiltered spectrum is due to light diffracted in the second order. By merging the two spectra, these distortions are avoided in the final full broadband spectrum. Although these distortions appear small in the overall lamp intensity, they can introduce large distortions in the white light reflectance, as will be shown in the next section.

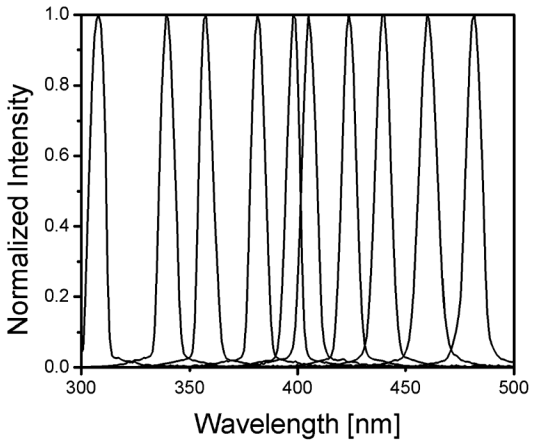

Figure 4: FastEEM laser excitation lines. There are ten laser lines from 308 to 480 nm spaced approximately every 10- 40 nm apart.

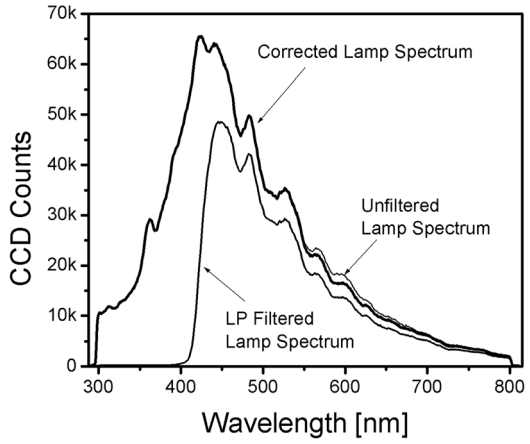

Figure 5: Spectrum of the FastEEM white light source (Xe Flashlamp) reflected off of a 20% reflectance standard. The corrected lamp spectrum represents the merging of two lamp spectra, the unfiltered lamp spectrum below 500 nm and the amplitude adjusted long pass (LP) filtered lamp spectra. This effectively avoids signals in the final spectra from light diffraction in the second order.

Rapid Reflectance Acquisition from Tissue Phantoms

To illustrate the performance of the FastEEM system in acquiring diffuse reflectance and single scattering spectra, we collected reflectance spectra from tissue phantoms. Tissue phantoms were constructed with solutions of polystyrene spheres in water (Polysciences Inc., Warrington, PA) to simulate scattering and hemoglobin (Sigma Chemicals, St. Louis, MO) to simulate absorption. We constructed four tissue phantoms of different diameter microspheres (d = 0.58, 0.771, 1.053, and 2.061 μm) with no Hb added and four tissue phantoms of one diameter microsphere (d = 1.053 μm) and four different physiological Hb concentrations ([Hb] = 0, 0.5, 1.0, and 2.0 mg/ml). The density of the spheres in the solutions were adjusted so that the phantoms represented physiological ranges of scattering ($\mu_s'(\lambda = 600\text{ nm}) \sim 1\text{-}2\ mm^{-1}$). The optical properties of such phantoms are easily characterized and have been used extensively to simulate tissue in the past (22).

Figure 6 illustrates the reflectance spectra acquired from tissue phantoms with varying hemoglobin concentrations using the FastEEM (d = 1.053 μm; $\mu_s'(\lambda = 600\text{ nm}) \sim 1\ mm^{-1}$; [Hb] = 0, 0.5, 1.0, 2.0 mg/ml). These spectra, acquired in 3 s along with a full EEM, exhibit very high SNR. The general shape of the reflectance spectra is a negatively sloped curve with a small ripple structure that rides on top. The bulk scattering properties of the phantom are responsible for the general sloping shape of the curve (diffuse scattering), while the ripple structure primarily originates from light that has been singly backscattered (see discussion below). The characteristic Hb absorption features are present in the reflectance spectra as the dips at approximately 420, 540, and 580 nm. As the Hb concentration increases, these dips become more pronounced. Therefore, one can see that the shape of these curves has information regarding the composition of the tissue phantom. Specifically, the depth and shape of the Hb dips contain information regarding the Hb concentration and oxygen saturation, while the overall slope of the curve and the size of the fine ripple structure contain information regarding the tissue's scattering features, and thus its morphological configuration.

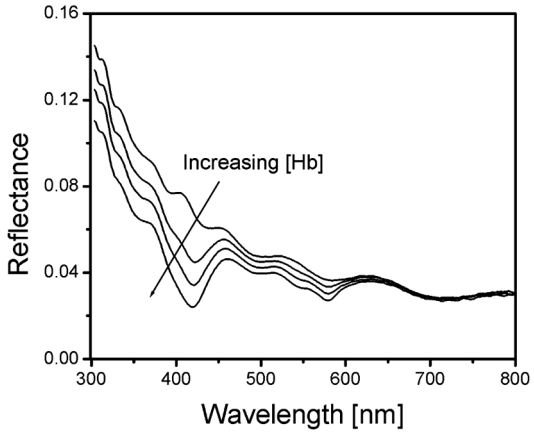

Figure 6: Reflectance spectra of tissue phantoms with increasing Hb concentrations (d = 1.053 μm; $\mu_s'(\lambda = 600\text{ nm}) \sim 1\ mm^{-1}$; [Hb] = 0, 0.5, 1.0, 2.0 mg/ml).

Figure 7 illustrates the white light reflectance spectra for a tissue phantom with no Hb added (d = 1.053 μm; $\mu_s'(\lambda = 600\text{ nm}) \sim 2\ mm^{-1}$; [Hb] = 0 mg/ml). The bold line indicates the calibrated reflectance spectrum acquired with the FastEEM. To illustrate the necessity of merging two white light spectra to avoid distortions from light diffracted in the second order, we also show the white light reflectance spectrum that has not been corrected (dashed line). Note the large distortions present between 550-800 nm. Also shown in Figure 7 is the

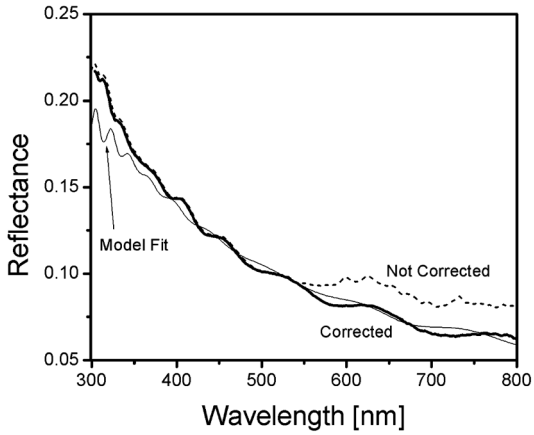

Figure 7: Reflectance spectra collected from a tissue phantom (d = 1.053 μm; $\mu_s'(\lambda = 600\text{ nm}) \sim 2\ mm^{-1}$; [Hb] = 0 mg/ml). The bold line indicates the reflectance spectra acquired with the FastEEM. The dotted line illustrates the distortions that are present if one doesn't remove light diffracted in the second order. The thin line is a diffuse reflectance model fit that represents the overall shape of the curve but does not duplicate the ripple structure that is due to singly backscattered light.

diffuse reflectance model calculation of the reflectance of the tissue phantom (5). Note that this model only represents the diffusely scattered photons. The measured reflectance signal includes the diffuse reflectance, as well as the LSS signal (i.e., those photons scattered in the backward direction). Therefore, the model fit accurately represents the broad shape of the reflectance; however, it does not duplicate the fine ripple structure in the reflectance spectrum and appears to deviate from the data in the blue region of the spectrum (300-400 nm). These differences can be accounted for by the singly-backscattered component of the reflected light as will be shown in the following measurements.

We measured the reflectance spectrum of the tissue phantoms of varying sphere diameters and used the diffuse reflectance model to simulate the reflectance of each of these phantoms. By subtracting the modeled diffuse reflectance from the reflectance data, we are left with a signal that represents the intensity of light that is scattered in the backward direction, which can be used to determine the size of the spheres in the top layer of the phantom (or in the case of tissue, the size of the nuclei in the epithelium) (20, 21). Figure 8 shows the residual obtained by subtracting the reflectance data from the diffuse reflectance model (R_{data}-R_{fit}). The frequency (in wavelength space) of the oscillations in these residuals increase with the diameter of the spheres, and therefore, they contain information on the size of the spheres (or nuclei in the case of tissue).

To illustrate that these residuals originate from light reflected in the backward direction, we plot, on the same wavelength axis, the backscattering cross section (differential scattering cross section in the exact backscattering direction, 180°) calculated using Mie theory for the corresponding sphere diameters. Note that these Mie calculations are approximations to the residuals seen in the figure since they have not accounted for the weighted angle of collection of the probe. In addition, the residuals shown in the figure may result from both single and multiple scattering (two or three or more scattering events) which are not well represented by the single Mie scattering cross sections. Nevertheless, the close match between the residuals and the Mie calculations illustrate that the probe design we have employed collects the backscattered component of the reflected light. The total collected reflectance consists of both the diffusely reflected light as well as a small component which is due to light scattered in the backward direction. It has been shown that these residual spectra can be used to determine the size of epithelial cell nuclei (20,21), one of the hallmarks of dysplastic change. For a more detailed discussion of the accuracy of the spectral algorithms to extract epithelial nuclear size distributions, we refer the reader to reference (20).

Rapid Fluorescence EEM Acquisition from Biochemicals

We measured a mixture of biochemicals with the FastEEM to illustrate its ability to accurately collect fluorescence EEM's. We fabricated a 3 ml solution of tryptophan (Sigma Aldrich, Princeton, NJ) and FAD (Sigma Aldrich, Princeton, NJ) in saline buffer (Sigma Aldrich, Princeton, NJ) at concentrations of 1 mg/ml and 0.5 mg/ml, respectively. Figure 9 shows the calibrated fluorescence EEM collected with the FastEEM. As can be seen from the figure, FAD exhibits a maximum emission at 525 nm, and the maximum excitation in the 450 nm

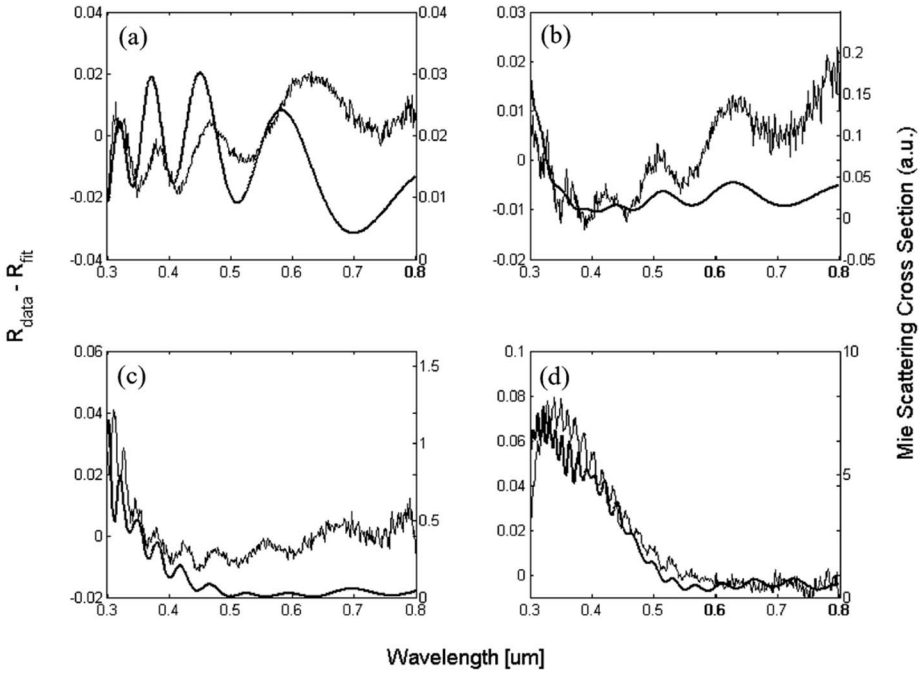

Figure 8: Backscattered component of the reflectance signal. Mie theory calculations are in bold, and the data is the thin line. Four bead diameters are shown: d = (**a**) 0.58 (**b**) 0.771 (**c**) 1.053 (**d**) 2.061 μm.

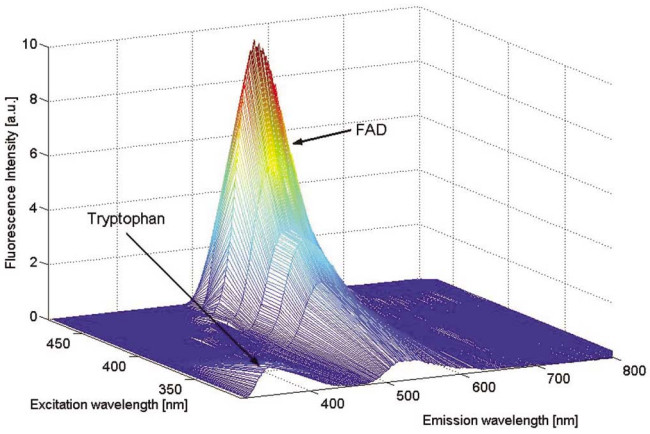

Figure 9: Excitation-Emission Matrix (EEM) of a mixture of fluorescent biochemicals (FAD and tryptophan). This EEM was measured using the FastEEM and was collected in 1.5 s. The large peak of FAD is clearly present with a maximum excitation at 450 nm and emission of 525 nm. Tryptophan is seen to be excited at 308 nm with a peak emission at 356 nm.

region, which is consistent with the literature (28). The maximum emission of tryptophan excited at 308 nm was measured by the FastEEM to be 356 nm, which closely matches the reported values of tryptophan emission of 353 nm (28).

These measurements illustrate the accuracy of the fluorescence EEM's measured with the FastEEM; however, it is likely that the concentrations of the fluorophore used in this study do not match those observed in epithelial dysplasia. Our preliminary studies measuring fluorescence EEM's in several types of epithelial dysplasia (uterine cervix, oral cavity, esophagus in both human and a Fisher rat model) indicate that the signal to noise ratio of measured tissue fluorescence is sufficiently high to distinguish tissue fluorophores such as porphyrins, NADH, collagen, and tryptophan.

Conclusion and Future Work

The new FastEEM system accurately acquires a fluorescence EEM and white light tissue reflectance for multimodal spectral analysis within a fraction of a second. The system has been optimized for use in a clinical setting. It is mobile, collects tissue spectra in the presence of ambient light, and acquires all tissue spectra within an acceptable time frame for clinical use.

The recent application of TMS has demonstrated the success of combining multiple spectroscopic modalities to determine a diagnosis. This technology is currently capable of characterizing a number of important physically relevant diagnostic parameters – contributions from collagen and NADH, nuclear size distribution and density, stromal scattering size and density, and hemoglobin concentration and oxygen saturation. As TMS further develops, identification

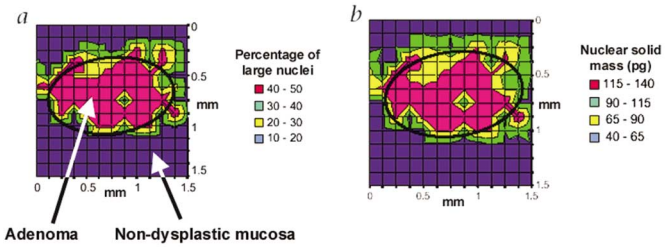

Figure 10: LSS images of a colon adenoma (31). Spatial distributions are shown for: (**a**) percentage of enlarged nuclei; (**b**) nuclear solid mass. The polyp borders are marked by ellipses. (Permission for reprinting this figure has been granted by the Nature Publishing Group.)

of new diagnostic parameters can be envisioned – contributions from porphyrins, FAD, tryptophan, as well as LSS methods to quantify distribution of sub-micron tissue structure in addition to cell nuclei.

This new instrument is now in a set of clinical studies in the oral cavity, the uterine cervix, and the gastrointestinal tract. As mentioned above, one major advantage of such technologies is their ability to provide a real-time diagnosis of disease. We are now acquiring learning data sets in each of the organs mentioned. We will then refine our spectral analysis algorithms and implement diagnostic algorithms for each of these organs to provide the physician with instant feedback on the disease state of the tissue. The software interface may provide the physician with the probability that a tissue site lies within a certain class of tissue (e.g., normal, low grade dysplasia, high grade dysplasia, or cancerous). The rate limiting step in providing a real-time spectral diagnosis is the diffuse reflectance spectral analysis, currently requiring on the order of two seconds for completion. As we accumulate larger learning data sets, we will report on the performance of these spectral and diagnostic algorithms.

Additional improvements in the system will include new optical fiber probe designs. It has recently been shown that polarization can be used to discriminate diffusely reflected light from singly backscattered light (29), and a new probe design has been implemented to collect polarized light *in vivo* (30). By proper arrangement of optical fibers, new probes can be envisioned that collect light scattered at certain narrow angle bands that may be able to more accurately discriminate nuclear size and other tissue parameters.

While this device provides detailed information about a small volume of tissue, there is a need to survey larger areas of tissue to identify regions of interest in a large field. Recently, a wide field imaging technique based on LSS has been shown to provide quantitative tissue information (31). LSS images are not conventional optical images. Rather, they are two dimensional maps of the spatial distributions of morphological parameters.

Gurjar *et al*. (31) created functional images of the percentage of enlarged nuclei and nuclear solid mass of separate colon polyps that grossly appeared identical under standard colonoscopy. Using the LSS imaging instrument, the dysplastic colon polyp could clearly be distinguished. The instrument (details can be found in reference (31)) collects multi-spectral images (11 narrow-bands, 4 nm FWHM, from 450-700 nm) of plane-polarized light (both parallel and perpendicular to the incident light) using a CCD. For each pixel (25 μm × 25 μm) of the imaged field (1.3 cm × 1.3 cm), a spectrum of light backscattered by the nuclei was first distinguished from the rest of the reflected light using polarization discrimination and then analyzed using the Mie theory-based computerized algorithm. The size and refractive index of the nuclei were obtained for each pixel. The imaged field was divided into 125 μm × 125 μm regions, and the percentage of nuclei larger than 10 microns and the mass of nuclear solids (e.g., chromatin content) were obtained for each of these areas.

The resulting images of the dysplastic colon polyp are shown in Figure 10. As expected, the nuclei are enlarged in the central, adenomatous region but not in the surrounding non-dysplastic tissue (panel a). Figure 10(b) illustrates the spatial distribution of the nuclear solid mass, displayed in units of picograms per nucleus. The nuclear solid mass in the region of the polyp is greater than that of the surrounding normal tissue, suggesting increased chromatin content (32, 33) and thus dysplasia in the region outlined. Both of these images present quantitative maps of tissue constituents indicative of dysplasia, providing an objective means for the surveillance of colonic precancerous lesions.

Spectral probes provide detailed morphological and biochemical information about the state of the tissue over a small (~1 mm diameter) region, from which an accurate diagnosis can be made. Wide area surveillance, by contrast, can image the full endoscopic field, but the spectral diagnostic information may be less specific. The two methods are complementary, suggesting the idea of a combined instrument where the wide-area spectral diagnostic image is superimposed on the white light image, and suspect areas are studied in greater detail with a contact probe. We are developing this type of integrated system to provide objective, detailed diagnostic information in real time, which will be used for in vivo diagnosis of dysplasia as well as a guide to biopsy to reduce sampling errors.

Acknowledgements

This work was conducted at the Massachusetts Institute of Technology Laser Biomedical Research Center under support of National Institute of Health grants P41-RR02594 and a Biomedical Research Partnership R01-CA97966.

References

1. H. Yoon, A. Martin, R. Benamouzig, E. Longchampt, J. Deyra, and S. Chaussade. Inter-observer Agreement on Histological Diagnosis of Colorectal Polyps: The APACC Study. *Gastroenterol. Clin. Biol. 26*, 220-224 (2002).
2. W. G. McCluggage, M. Y. Walsh, C. M. Thornton, P. W. Hamilton, A. Date, L. M. Caughley, and H. Bharucha. Inter- and Intra-observer Variation in the Histopathological Reporting of Cervical Squamous Intraepithelial Lesions using a Modified Bethesda Grading System. *Br. J. Obstet. Gynaecol. 105*, 206-210 (1998).
3. S. M. Ismail, A. B. Colclough, J. S. Dinnen, D. Eakins, D. M. Evans, E. Gradwell, J. P. O'Sullivan, J. M. Summerell, and R. Newcombe. Reporting Cervical Intra-epithelial Neoplasia (CIN): Intra- and Interpathologist Variation and Factors Associated with Disagreement. *Histopathology 16*, 371-376 (1990).
4. B. J. Reid, R. C. Haggitt, C. E. Rubin, G. Roth, C. M. Surawicz, G. Van Belle, K. Lewin, W. M. Weinstein, D. A. Antonioli, and H. Goldman. Observer Variation in the Diagnosis of Dysplasia in Barrett's Esophagus. *Hum. Pathol. 19*, 166-178 (1988).
5. G. Zonios, L. T. Perelman, V. Backman, R. Manoharan, M. Fitzmaurice, J. Van Dam, and M. S. Feld. Diffuse Reflectance Spectroscopy of Human Adenomatous Colon Polyps *In Vivo*. *Appl. Opt. 38*, 6628-6637 (1999).
6. I. Georgakoudi, B. C. Jacobson, J. Van Dam, V. Backman, M. B. Wallace, M. G. Muller, Q. Zhang, K. Badizadegan, D. Sun, G. A. Thomas, L. T. Perelman, and M. S. Feld. Fluorescence, Reflectance, and Light-scattering Spectroscopy for Evaluating Dysplasia in Patients with Barrett's Esophagus. *Gastroenterology 120*, 1620-1629 (2001).
7. I. Georgakoudi, E. E. Sheets, M. G. Muller, V. Backman, C. P. Crum, K. Badizadegan, R. R. Dasari, and M. S. Feld. Trimodal Spectroscopy for the Detection and Characterization of Cervical Precancers *In Vivo*. *Am. J. Obstet. Gynecol. 186*, 374-382 (2002).
8. J. R. Mourant, I. J. Bigio, J. Boyer, R. L. Conn, T. Johnson, and T. Shimada. Spectroscopic Diagnosis of Bladder Cancer with Elastic Light Scattering. *Lasers Surg. Med. 17*, 350-357 (1995).
9. J. B. Fishkin, O. Coquoz, E. R. Anderson, M. Brenner, and B. J. Tromberg. Frequency-domain Photon Migration Measurements of Normal and Malignant Tissue Optical Properties in a Human Subject. *Appl. Opt. 36*, 10-20 (1995).
10. I. J. Bigio and J. R. Mourant. Ultraviolet and Visible Spectroscopies for Tissue Diagnostics: Fluorescence Spectroscopy and Elastic-scattering Spectroscopy. *Phys. Med. Biol. 42*, 803-814 (1997).
11. M. F. Mitchell, S. B. Cantor, N. Ramanujam, G. Tortolero-Luna, and R. Richards-Kortum. Fluorescence Spectroscopy for Diagnosis of Squamous Intraepithelial Lesions of the Cervix. *Obstet. Gynecol. 93*, 462-470 (1999).
12. I. Georgakoudi, B. C. Jacobson, M. G. Muller, E. E. Sheets, K. Badizadegan, D. L. Carr-Locke, C. P. Crum, C. W. Boone, R. R. Dasari, J. Van Dam, and M. S. Feld. NAD(P)H and Collagen as *In Vivo* Quantitative Fluorescent Biomarkers of Epithelial Precancerous Changes. *Cancer Res. 62*, 682-687 (2002).
13. G. S. Fiarman, M. H. Nathanson, A. B. West, L. I. Deckelbaum, L. Kelly, and C. R. Kapadia. Differences in Laser-induced Autofluorescence Between Adenomatous and Hyperplastic Polyps and Normal Colonic Mucosa by Confocal Microscopy. *Dig. Dis. Sci. 40*, 1261-1268 (1995).
14. T. Vo-Dinh, M. Panjehpour, and B. F. Overholt. Laser-induced Fluorescence for Esophageal Cancer and Dysplasia Diagnosis. *Ann. N. Y. Acad. Sci. 838*, 116-122 (1998).
15. S. P. Schantz, V. Kolli, H. E. Savage, G. Yu, J. P. Shah, D. E. Harris, A. Katz, R. R. Alfano, and A. G. Huvos. *In Vivo* Native Cellular Fluorescence and Histological Characteristics of Head and Neck Cancer. *Clin. Cancer Res. 4*, 1177-1182 (1998).

16. M. G. Muller, T. A. Valdez, I. Georgakoudi, V. Backman, C. Fuentes, S. Kabani, N. Laver, Z. Wang, C. W. Boone, R. R. Dasari, S. M. Shapshay, and M. S. Feld. Spectroscopic Detection and Evaluation of Morphologic and Biochemical Changes in Early Human Oral Carcinoma. *Cancer 97*, 1681-1692 (2003).
17. M. Rajadhyaksha, R. R. Anderson, and R. H. Webb. Video-rate Confocal Scanning Laser Microscope for Imaging Human Tissues *In Vivo*. *Appl. Opt. 38*, 2105-2115 (1999).
18. W. Denk, J. H. Strickler, and W. W. Webb. Two-photon Laser Scanning Fluorescence Microscopy. *Science 248*, 73-76 (1990).
19. D. Huang, E. A. Swanson, C. P. Lin, J. S. Schuman, W. G. Stinson, W. Chang, M. R. Hee, T. Flotte, K. Gregory, and C. A. Puliafito. Optical Coherence Tomography. *Science 254*, 1178-1181 (1991).
20. L. T. Perelman, V. Backman, M. B. Wallace, G. Zonios, R. Manoharan, A. Nusrat, S. Shields, M. Seiler, C. Lima, T. Hamano, I. Itzkan, J. Van Dam, J. M. Crawford, and M. S. Feld. Observation of Periodic Fine Structure in Reflectance from Biological Tissue: A New Technique for Measuring Nuclear Size Distribution. *Phys. Rev. Lett. 80*, 627-630 (1998).
21. V. Backman, M. B. Wallace, L. T. Perelman, J. T. Arendt, R. Gurjar, M. G. Muller, Q. Zhang, G. Zonios, E. Kline, J. A. McGilligan, S. Shapshay, T. Valdez, K. Badizadegan, J. M. Crawford, M. Fitzmaurice, S. Kabani, H. S. Levin, M. Seiler, R. R. Dasari, I. Itzkan, J. Van Dam, M. S. Feld, and T. McGillican. Detection of Preinvasive Cancer Cells. *Nature 406*, 35-36 (2000).
22. M. G. Muller, I. Georgakoudi, Q. Zhang, J. Wu, and M. S. Feld. Intrinsic Fluorescence Spectroscopy in Turbid Media: Disentangling Effects of Scattering and Absorption. *Applied Optics 40*, 4633-4646 (2001).
23. Q. Zhang, M. G. Muller, J. Wu, and M. S. Feld. Turbidity-free Fluorescence Spectroscopy of Biological Tissue. *Opt. Lett. 25*, 1451-1453 (2000).
24. J. Wu, M. S. Feld, and R. P. Rava. Analytical Model for Extracting Intrinsic Fluorescence in Turbid Media. *Appl. Opt. 32*, 3585-3595 (1993).
25. A. Talvensaari, M. Apaja-Sarkkinen, M. Hoyhtya, A. Westerlund, U. Puistola, and T. Turpeenniemi. Matrix Metalloproteinase 2 Immunoreactive Protein Appears Early in Cervical Epithelial Dedifferentiation. *Gynecol. Oncol. 72*, 306-311 (1999).
26. R. A. Zangaro, L. Silveira, R. Manoharan, G. Zonios, I. Itzkan, R. R. Dasari, J. Van Dam, and M. S. Feld. Rapid Multiexcitation Fluorescence Sepectroscopy System for *In Vivo* Tissue Diagnosis. *Appl. Opt. 35*, 5211-5219 (1996).
27. M. G. Muller, A. Wax, I. Georgakoudi, R. R. Dasari, and M. S. Feld. A Reflectance Spectrofluorimeter for Real-time Spectral Diagnosis of Disease. *Rev. Sci. Instr. 73*, 3933-3937 (2002).
28. J. R. Lackowicz. *Principle of Fluorescence Spectroscopy*. Kluwer Academic/Plenum, New York (1999).
29. V. Backman, V. Gopal, M. Kalashnikov, K. Badizadegan, R. Gurjar, A. Wax, I. Georgakoudi, M. G. Muller, C. W. Boone, R. R. Dasari, and M. S. Feld. Measuring Cellular Structure at Submicrometer Scale with Light Scattering Spectroscopy. *IEEE J. Sel. Top. Quant. Elect. 7*, 887-893 (2001).
30. A. Myakov, L. Nieman, L. Wicky, U. Utzinger, R. Richards-Kortum, and K. Sokolov. Fiber Optic Probe for Polarized Reflectance Spectroscopy *In Vivo*: Design and Performance. *J. Biomed. Opt. 7*, 388-397 (2002).
31. R. S. Gurjar, V. Backman, L. T. Perelman, I. Georgakoudi, K. Badizadegan, I. Itzkan, R. R. Dasari, and M. S. Feld. Imaging Human Epithelial Properties with Polarized Light-scattering Spectroscopy. *Nat. Med. 7*, 1245-1248 (2001).
32. G. L. Brown, M. McEwan, and M. Pratt. Macromolecular Weight and Size of Deoxypentose Nucleic Acids. *Nature 176*, 161-162 (1955).
33. H. G. Davies, E. M. Deeley, and E. F. Denby. Attempts at Measurement of Lipid, Nucleic Acid and Protien Content of Cell Nuclei by Microscope-interferometry. *Exp. Cell Res. Suppl. 4*, 136-149 (1957).

Date Received: October 24, 2003